Vehicle System Dynamics

International Journal of Vehicle Mechanics and Mobility

ISSN: 0042-3114 (Print) 1744-5159 (Online) Journal homepage: www.tandfonline.com/journals/nvsd20

Optimal control of a NASCAR – specification race car

D. J. N. Limebeer, M. Bastin, E. Warren & H. G. Fensham

VEHICLE SYSTEM DYNAMICS
2023, VOL. 61, NO. 5, 1210–1235
https://doi.org/10.1080/00423114.2022.2067573

OPEN ACCESS Check for updates

Optimal control of a NASCAR – specification race car

D. J. N. Limebeer [a], M. Bastin[b], E. Warren[b] and H. G. Fensham[a]

[a]School of Electrical and Information Engineering, Faculty of Engineering and the Built Environment, University of the Witwatersrand, Johannesburg, South Africa; [b]Richard Childress Racing, Welcome, NC, USA

ABSTRACT
This paper adapts the minimum-lap-time simulation technologies developed in Formula One to NASCAR. The adaptation process requires recognition of the variable lateral curvature of some tracks, as well as the asymmetries of NASCAR-specification race cars that have been configured for high-speed oval tracks that are dominated by left-hand cornering. These asymmetries include different suspension characteristics on the left- and right-hand ends of each axle, different left- and right-hand tyres on each axle, as well as asymmetries in the car's aerodynamic performance. The results compare optimal control calculations, industrial simulation-based predictions and race-captured telemetry data. For the most part, these various data sources are in good agreement, with the importance of variable lateral camber highlighted. It is demonstrated how race car drivers have to find the best compromise between the conflicting objectives of exploiting the additional camber available on the outside of variable-camber tracks and increasing the travelled distance and racing line cornering curvature.

ARTICLE HISTORY
Received 20 September 2021
Revised 5 March 2022
Accepted 13 April 2022

KEYWORDS
Minimum lap-time simulation; optimal control; vehicle modelling; high-fidelity simulation; three-dimensional tracks; NASCAR

1. Introduction

Much has been written about the use of optimal control in closed-circuit racing, with early attempts to predict the lap-time performance of road vehicles dating back to the late 1950s. An example of this type is discussed in [1] in relation to the Monza circuit in Italy. In 1971, a computer analysis of the Watkins Glen GP circuit (USA) was carried out with the goal of computing the speed and acceleration profiles of race cars [2]. Early minimum lap time simulations using predefined trajectories and quasi-steady-state models are considered in [3]. A related approach to computing the optimal trajectory is discussed in [4]. This paper considers a constrained optimisation problem that recognises the geometry of the circuit and the dynamics of the vehicle. A more sophisticated procedure for optimising a vehicle's performance by solving a (nonlinear) optimal control problem (OCP) is presented in [5]. The goal is to minimise the manoeuvre time while satisfying the dynamic equations describing the vehicle, and the road boundaries. A minimum manoeuvre time problem for a hairpin curve at the Fuji Speedway (Japan) is considered in

CONTACT D. J. N. Limebeer david.limebeer@wits.ac.za, david.limebeer@eng.ox.ac.uk

[6]. Unlike some earlier studies no pre-assigned reference trajectory is imposed – the trajectory is determined by the optimiser. A single-track three DOF car model is employed (the well-known 'bicycle model'). The solution of the OCP is obtained using a sequential conjugate-gradient-restoration algorithm [7,8]. A twin-track (four-wheeled) vehicle model is introduced in [9], which has three degrees of freedom. The inputs are the steering rate and the total drive/braking longitudinal force. The OCP is solved by an indirect gradient projection method [10]. In [11], a seven DOF planar car model is employed, which includes the standard longitudinal, lateral and yaw motions of the car's chassis, and the spin motion of the four wheels. The tyre forces depend on their slips and normal loads through Magic Formulae. The sequential-quadratic-programming algorithm is used to solve the OCP. Another minimum lap time simulation problem for race cars is reported in [12]. In this case, an interior-point feasible sequential quadratic programming code [13] is used with forward-finite-difference gradient calculations. In [14], the car is represented by a two-track model operating under quasi-steady-state conditions, but with the racing line free to be determined by the optimiser. The lap time of a race series-hybrid electric vehicle is considered in [15]. The powertrain considered contains an internal combustion engine, a motor-generator system and a battery. In 2011, a survey of automotive optimal control was published [16], with the third section devoted to minimum-time manoeuvring. Much of the recent literature is reviewed in [17], with additional source material available in [18].

The aforementioned literature focusses primarily on symmetric cars (matched tyres and suspensions on each axle) operating on tracks with zero or only moderate camber that can be assumed laterally constant. The track inclination is also assumed constant in the lateral direction. Formula One cars race on both street and purpose-built race circuits that are either clockwise, anti-clockwise, or a combination of both. For example, Monza is a clockwise racing circuit, while Baku City is an anti-clockwise street circuit. The Suzuka Grand Prix circuit in Japan is clockwise for the first half, and then anti-clockwise for the second half – the change in sense is achieved with a mid-circuit over-under pass. Of note is the fact that Formula One cars are expected to make left- and right-handed turns in roughly equal measure.

In contrast with most Formula One tracks, NASCAR ovals are heavily banked and dominated by left-hand cornering. NASCAR races also run on road courses, with the Circuit of the Americas track shared with Formula One. Some NASCAR circuits also have a significant variation in their lateral camber – examples include the Darlington and Bristol Motor Speedways. The differences between Formula One tracks and NASCAR ovals have produced new challenges in both track and car modelling, and the corresponding vehicle control. In the case of track modelling, variable lateral and longitudinal curvature was introduced [19], which is a natural outgrowth of the constant-camber ribbon models detailed in [18,20,21]. The cars are different too. As a result of their asymmetric setup for oval circuits, the right- and left-hand tyres on each axles have different properties and operate under very different loading conditions. These tyre asymmetries extend to the left- and right-hand side suspension systems as well as the car's aerodynamic properties.

The purpose of this paper is to develop high-fidelity track and car models for a heavily banked NASCAR oval with variable lateral curvature, and study the associated minimum-time vehicular OCP. We will consider a typical NASCAR race car run on the Darlington Raceway. As can be seen from Figure 1(a), Darlington is an egg-shaped oval with the cars circulating in an anti-clockwise direction. This figure also illustrates the fact that the circuit

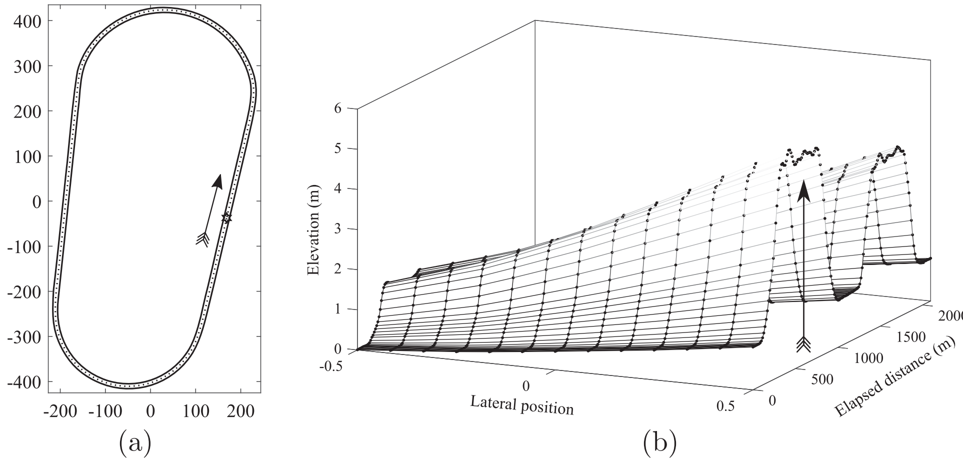

Figure 1. Darlington Raceway, Darlington, South Carolina. The (a) part of the figure shows the circuit, the start-finish line and the racing direction. The (b) part of the figure shows a surface plot of the Darlington Raceway with the corresponding LiDAR survey data points.

is highly banked, with lateral camber variations particularity evident in Turn 2 ($\approx$700 m from the start-finish line); see the vertical arrow on the (b) part of the figure; at this point, the lateral track-surface camber variation is approximately 10°. Each of the four turns is left-handed and the lap distance is approximately 2095 m. The outer boundary of the track varies by approximately 4.49 m in elevation, while the elevation of the inner boundary varies by about 1.31 m.

Section 2 contains an overview of recent road modelling results for closed-circuit racing tracks with variable lateral curvature [19,22]. Fitting curvature functions to measured survey data can be configured as a secondary OCP [17–19,21]. Appendix 1 addresses the problem of changing the car's circulation direction relative to the track survey data. The car model is an extension of that described in [18] and is described in Section 4. The car and tyre parameters are given in Appendix 2, with the aerodynamic coefficients described in Appendix 3. The car's chassis configuration is described in Appendix 4, with the suspension preload setup detailed in Appendix 5. The minimum-time and track modelling OCP are both solved as numerical optimisation problems based on *hp*-adaptive Gaussian quadrature collocation [23]. The solution methodology for the minimum lap time problem is given in Section 5. The results are given in Section 6, with conclusions drawn in Section 7.

2. Road modelling

Differential-geometric methods have been used in a wide variety of rolling-contact problems. In the context of vehicle dynamics, an early application of curvilinear coordinates was in a 2D setting in motorcycle work [24]. These ideas were then extended to 3D road models in [20,21], where the road was represented as a geometric ribbon. These ideas are subsequently extended in [19] to tracks with more general features such as lateral curvature variations. Some interesting recent work [22], that is related to [19], will now be reviewed and extended.

2.1. Background

As with most road-car modelling exercises, one requires several frames of reference – the first two are the inertial frame $[\boldsymbol{e}_x^g, \boldsymbol{e}_y^g, \boldsymbol{e}_z^g]$ and the car body-fixed frame $[\boldsymbol{e}_x^b, \boldsymbol{e}_y^b, \boldsymbol{e}_z^b]$. Suppose vector $\boldsymbol{x}^b$ is fixed in a rotating body-fixed frame, then it can also be expressed in the inertial frame as $\boldsymbol{x}^g = R\boldsymbol{x}^b$ for some time-varying rotation matrix R. It then follows that

$$\begin{aligned} \dot{\boldsymbol{x}}^g &= \dot{R}\boldsymbol{x}^b \\ &= \dot{R}R^T\boldsymbol{x}^g \\ &= R(R^T\dot{R})R^T\boldsymbol{x}^g \\ \Rightarrow \dot{\boldsymbol{x}}^b &= (R^T\dot{R})\boldsymbol{x}^b, \end{aligned} \tag{1}$$

where $R^T\dot{R}$ is a skew-symmetric matrix representation of the angular velocity vector of the body-fixed frame; these arguments are developed in detail in [25]. It now follows that for each body-fixed basis vector

$$\begin{bmatrix} \dot{\boldsymbol{e}}_x^b & \dot{\boldsymbol{e}}_y^b & \dot{\boldsymbol{e}}_z^b \end{bmatrix} = \begin{bmatrix} \boldsymbol{e}_x^b & \boldsymbol{e}_y^b & \boldsymbol{e}_z^b \end{bmatrix} \begin{bmatrix} 0 & -\omega_z^b & \omega_y^b \\ \omega_z^b & 0 & -\omega_x^b \\ -\omega_y^b & \omega_x^b & 0 \end{bmatrix}. \tag{2}$$

The third frame we require is the Darboux frame $[\boldsymbol{t}, \boldsymbol{n}, \boldsymbol{m}]$ that travels along the track centre line [18] (see Figure 2(a)). The track's centre-line curvature is assumed to be $\boldsymbol{\Omega}^b(s) = [\Omega_x^b \;\; \Omega_y^b \;\; \Omega_z^b]^T(s)$, which is a function of the elapsed distance s along the centre line. An orthogonal basis for the Darboux frame is given by the columns of the rotation matrix [21]

$$R = R_z(\theta)R_y(\mu)R_x(\phi) = \begin{bmatrix} c_\theta c_\mu & c_\theta s_\mu s_\phi - s_\theta c_\phi & c_\theta s_\mu c_\phi + s_\theta s_\phi \\ s_\theta c_\mu & s_\theta s_\mu s_\phi + c_\theta c_\phi & s_\theta s_\mu c_\phi - c_\theta s_\phi \\ -s_\mu & c_\mu s_\phi & c_\mu c_\phi \end{bmatrix}, \tag{3}$$

in which $R_x(\phi)$, $R_y(\mu)$ and $R_z(\theta)$ represent, respectively, rotations around x, y and z axes. The Euler angles θ, μ and ϕ represent the yaw, inclination and camber angles of the road; 's' and 'c' refer to the sine and cosine of the corresponding (subscripted) quantities. The unit basis vectors $[\boldsymbol{t}, \boldsymbol{n}, \boldsymbol{m}]$ (see Figure 2) are given by the first, second and third columns of R, respectively. The Euler angles and the angular rates are related to the angular velocity of the Darboux frame by Perantoni and Limebeer [21]:

$$\begin{bmatrix} \Omega_x^b \\ \Omega_y^b \\ \Omega_z^b \end{bmatrix} = \begin{bmatrix} 1 & 0 & -s_\mu \\ 0 & c_\phi & c_\mu s_\phi \\ 0 & -s_\phi & c_\mu c_\phi \end{bmatrix} \begin{bmatrix} \phi' \\ \mu' \\ \theta' \end{bmatrix}; \tag{4}$$

Ω^b is expressed in the Darboux frame. To avoid notational clutter, Ω^b and its components will be expressed as just Ω in the sequel. A skew-symmetric representation of the Darboux frame's angular velocity (expressed in rad/m) is given by $R^T\dot{R}$ [18,21]; in this context, the

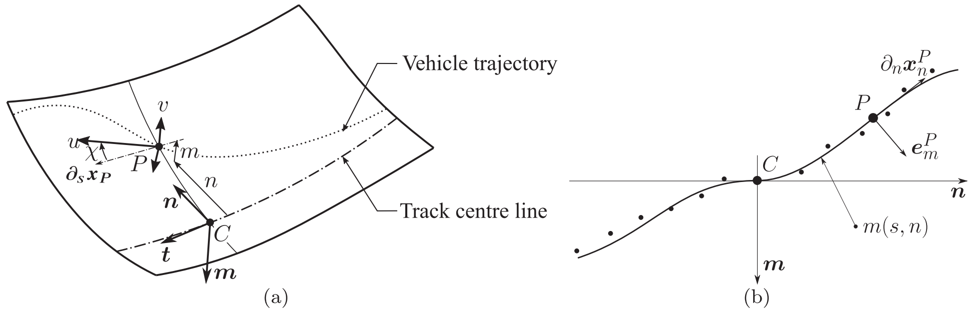

Figure 2. (a) Three-dimensional road patch and the car's position on it. (b) Road cross-section represented by $m(s, n)$, with LiDAR data points.

'dot' represents a derivative with respect to s. The location of the (moving) origin of the Darboux frame is given by

$$\begin{bmatrix} x_C \\ y_C \\ z_C \end{bmatrix} = \int \boldsymbol{t} \mathrm{d}s = \int \begin{bmatrix} c_\phi c_\mu \\ s_\phi c_\mu \\ -s_\mu \end{bmatrix} \mathrm{d}s. \tag{5}$$

3. Road geometry

Suppose that a general point on the road surface, expressed in inertial coordinates, is

$$\boldsymbol{x}_P(s, n) = x(s, n)\boldsymbol{e}_x^g + y(s, n)\boldsymbol{e}_y^g + z(s, n)\boldsymbol{e}_z^g, \tag{6}$$

where the parametric variables are s, the distance travelled along the centre line, and n, the distance from the track's centre line. Two rather than three independent variables are required, because $\boldsymbol{x}_P(s, n)$ is constrained to the road surface. Following [19], let us suppose that the road surface is given by $m(s, n)$, which represents height variations relative to the tangent plane at point C (see Figure 2(b)). This means that a general point on the road surface is described in Darboux coordinates by

$$\mathcal{S} = \left\{ \boldsymbol{x}_P(s, n) = \int \boldsymbol{t}\mathrm{d}s + \boldsymbol{n}(s)n + \boldsymbol{m}(s)m(s, n) \in \mathbb{R}^3 : s \in [s_i, s_f], n \in \frac{1}{2}[-r_w, r_w] \right\}. \tag{7}$$

In vehicular applications, the vector $\boldsymbol{x}_P$ is the location of the car's reference point on the road surface, and $\boldsymbol{x}_C = \int \boldsymbol{t}\mathrm{d}s$ is the position of the origin of the Darboux frame (on the centre line). See points P and C in Figure 2. The vehicle's trajectory is assumed to start at s_i and end at s_f. The lateral position of P with respect to the centre line is n (in Darboux coordinates). It is assumed that the road width r_w is variable and a function of s. We can define vectors $\partial_s \boldsymbol{x}_P$ and $\partial_n \boldsymbol{x}_P$, which define the plane tangent to the road surface in the neighbourhood of P. The car's heading angle χ is the angle between $\boldsymbol{e}_x^b$ and $\partial_s \boldsymbol{x}_P$ – this is not the same as the heading angle defined in the prior literature, which is the angle between $\boldsymbol{e}_x^b$ and $\boldsymbol{t}$ [20,21]. For mathematical convenience, we will assume that the road surface is *regular* [26], this ensures that $\partial_s \boldsymbol{x}_P$ and $\partial_n \boldsymbol{x}_P$ are non-zero and linearly independent (but not necessarily orthogonal). A unit normal to the surface at P is given by

$$\boldsymbol{e}_m^P = \frac{\partial_s \boldsymbol{x}_P \times \partial_n \boldsymbol{x}_P}{\|\partial_s \boldsymbol{x}_P \times \partial_n \boldsymbol{x}_P\|}. \tag{8}$$

We will assume that the road surface normal at $\boldsymbol{x}_P$ is parallel to the body-fixed z-axis, that is,

$$\boldsymbol{e}_z^b = \boldsymbol{e}_m^P. \tag{9}$$

It follows from (8) and (9) that

$$\boldsymbol{e}_z^b.\partial_s \boldsymbol{x}_P = 0, \tag{10}$$

$$\boldsymbol{e}_z^b.\partial_n \boldsymbol{x}_P = 0. \tag{11}$$

These constraint equations restrict the car to a single rotational freedom (around the surface normal), which we will now examine. A plan view of the contact point P and its surrounding contact patch is given in Figure 3. From this figure, one can immediately deduce that

$$\cos\chi = \frac{\boldsymbol{e}_x^b.\partial_s \boldsymbol{x}_P}{\|\partial_s \boldsymbol{x}_P\|} \quad \text{and} \quad \sin\chi = -\frac{\boldsymbol{e}_y^b.\partial_s \boldsymbol{x}_P}{\|\partial_s \boldsymbol{x}_P\|} \tag{12}$$

and

$$\cos\xi = \frac{\boldsymbol{e}_y^b.\partial_n \boldsymbol{x}_P}{\|\partial_n \boldsymbol{x}_P\|} \quad \text{and} \quad \sin\xi = \frac{\boldsymbol{e}_x^b.\partial_n \boldsymbol{x}_P}{\|\partial_n \boldsymbol{x}_P\|}. \tag{13}$$

It is also evident that

$$\xi = \frac{\pi}{2} - \arccos\left(\frac{\partial_s \boldsymbol{x}_P.\partial_n \boldsymbol{x}_P}{\|\partial_s \boldsymbol{x}_P\|.\|\partial_n \boldsymbol{x}_P\|}\right) + \chi. \tag{14}$$

When $\partial_s \boldsymbol{x}_P$ and $\partial_n \boldsymbol{x}_P$ are orthogonal $\xi = \chi$. It is nicely demonstrated in [22] that

$$\dot{\chi} = \omega_z^b + \frac{(\partial_{ss} \boldsymbol{x}_P \times \partial_s \boldsymbol{x}_P).\boldsymbol{e}_m^p}{\partial_s \boldsymbol{x}_P.\partial_s \boldsymbol{x}_P}\dot{s} + \frac{(\partial_{sn} \boldsymbol{x}_P \times \partial_s \boldsymbol{x}_P).\boldsymbol{e}_m^p}{\partial_s \boldsymbol{x}_P.\partial_s \boldsymbol{x}_P}\dot{n}. \tag{15}$$

A similar calculation shows that

$$\dot{\xi} = \omega_z^b + \frac{(\partial_{sn} \boldsymbol{x}_P \times \partial_n \boldsymbol{x}_P).\boldsymbol{e}_m^p}{\partial_n \boldsymbol{x}_P.\partial_n \boldsymbol{x}_P}\dot{s} + \frac{(\partial_{nn} \boldsymbol{x}_P \times \partial_n \boldsymbol{x}_P).\boldsymbol{e}_m^p}{\partial_n \boldsymbol{x}_P.\partial_n \boldsymbol{x}_P}\dot{n}. \tag{16}$$

In view of (14), one of (15) and (16) is mathematically redundant, but both are retained for computational purposes.

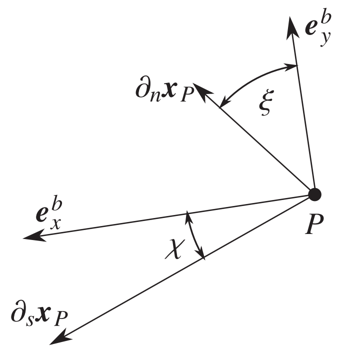

Figure 3. Heading angle χ and heading co-angle ξ.

3.1. Translational velocity constraint

Our purpose here is to relate the parametric and body-fixed linear velocities. The velocity of P is given by

$$\frac{\mathrm{d}}{\mathrm{d}t}\boldsymbol{x}_P = \partial_s \boldsymbol{x}_P \dot{s} + \partial_n \boldsymbol{x}_P \dot{n}, \tag{17}$$

which means that

$$\partial_s \boldsymbol{x}_P \dot{s} + \partial_n \boldsymbol{x}_P \dot{n} = u\boldsymbol{e}_x^b + v\boldsymbol{e}_y^b + w\boldsymbol{e}_z^b, \tag{18}$$

where u, v and w are the body-fixed components of the car's linear velocity. Dotting this equation with $\boldsymbol{e}_z^b$ shows that

$$w = 0, \tag{19}$$

since each of the remaining vectors is in the plane tangent to the road surface. We can now dot (18) with $\partial_s \boldsymbol{x}_P$ and $\partial_n \boldsymbol{x}_P$, while recognising (19), to obtain

$$\begin{bmatrix} \partial_s \boldsymbol{x}_P.\partial_s \boldsymbol{x}_P & \partial_s \boldsymbol{x}_P.\partial_n \boldsymbol{x}_P \\ \partial_n \boldsymbol{x}_P.\partial_s \boldsymbol{x}_P & \partial_n \boldsymbol{x}_P.\partial_n \boldsymbol{x}_P \end{bmatrix} \begin{bmatrix} \dot{s} \\ \dot{n} \end{bmatrix} = \begin{bmatrix} \partial_s \boldsymbol{x}_P.\boldsymbol{e}_x^b & \partial_s \boldsymbol{x}_P.\boldsymbol{e}_y^b \\ \partial_n \boldsymbol{x}_P.\boldsymbol{e}_x^b & \partial_n \boldsymbol{x}_P.\boldsymbol{e}_y^b \end{bmatrix} \begin{bmatrix} u \\ v \end{bmatrix}. \tag{20}$$

In conformity with standard differential-geometric notation,

$$I = \begin{bmatrix} \partial_s \boldsymbol{x}_P.\partial_s \boldsymbol{x}_P & \partial_s \boldsymbol{x}_P.\partial_n \boldsymbol{x}_P \\ \partial_n \boldsymbol{x}_P.\partial_s \boldsymbol{x}_P & \partial_n \boldsymbol{x}_P.\partial_n \boldsymbol{x}_P \end{bmatrix} \tag{21}$$

is called the *first fundamental form*, which facilitates the calculation of metric properties such as 'length'. It follows from (12) and (13) that

$$J = \begin{bmatrix} \partial_s \boldsymbol{x}_P.\boldsymbol{e}_x^b & \partial_s \boldsymbol{x}_P.\boldsymbol{e}_y^b \\ \partial_n \boldsymbol{x}_P.\boldsymbol{e}_x^b & \partial_n \boldsymbol{x}_P.\boldsymbol{e}_y^b \end{bmatrix} = \begin{bmatrix} \cos\chi \, \|\partial_s \boldsymbol{x}_P\| & -\sin\chi \, \|\partial_s \boldsymbol{x}_P\| \\ \sin\xi \, \|\partial_n \boldsymbol{x}_P\| & \cos\xi \, \|\partial_n \boldsymbol{x}_P\| \end{bmatrix}, \tag{22}$$

and so

$$\begin{bmatrix} \dot{s} \\ \dot{n} \end{bmatrix} = I^{-1} J \begin{bmatrix} u \\ v \end{bmatrix}, \tag{23}$$

constrains the way in which $\dot{s}$ and $\dot{n}$ can evolve given $\dot{u}$ and $\dot{v}$. The assumed regularity of the road surface implies the invertibility of I [26].

3.2. Angular velocity constraint

Since the car is assumed to have no suspension, its roll and pitch motions are dictated by the road surface. This suggests a nonholonomic constraint that governs ω_x^b and ω_y^b given u and v. Differentiating (10) and (11) with respect to time gives

$$0 = \frac{\mathrm{d}}{\mathrm{d}t}(\boldsymbol{e}_z^b).\partial_s \boldsymbol{x}_P + \boldsymbol{e}_z^b.\frac{\mathrm{d}}{\mathrm{d}t}(\partial_s \boldsymbol{x}_P), \tag{24}$$

$$0 = \frac{\mathrm{d}}{\mathrm{d}t}(\boldsymbol{e}_z^b).\partial_n \boldsymbol{x}_P + \boldsymbol{e}_z^b.\frac{\mathrm{d}}{\mathrm{d}t}(\partial_n \boldsymbol{x}_P). \tag{25}$$

Eliminating the $\frac{\mathrm{d}}{\mathrm{d}t}(\boldsymbol{e}_z^b)$ terms using (2) and expanding the time derivatives of the partial derivative terms gives

$$\left(\begin{bmatrix} \partial_s \boldsymbol{x}_P \\ \partial_n \boldsymbol{x}_P \end{bmatrix} . \begin{bmatrix} \boldsymbol{e}_x^b & \boldsymbol{e}_y^b \end{bmatrix} = J\right) \begin{bmatrix} -\omega_y^b \\ \omega_x^b \end{bmatrix} = \begin{bmatrix} \boldsymbol{e}_m^P.\partial_{ss}\boldsymbol{x}_P & \boldsymbol{e}_m^P.\partial_{sn}\boldsymbol{x}_P \\ \boldsymbol{e}_m^P.\partial_{ns}\boldsymbol{x}_P & \boldsymbol{e}_m^P.\partial_{nn}\boldsymbol{x}_P \end{bmatrix} \begin{bmatrix} \dot{s} \\ \dot{n} \end{bmatrix}, \tag{26}$$

where

$$II = \begin{bmatrix} \boldsymbol{e}_m^P.\partial_{ss}\boldsymbol{x}_P & \boldsymbol{e}_m^P.\partial_{sn}\boldsymbol{x}_P \\ \boldsymbol{e}_m^P.\partial_{ns}\boldsymbol{x}_P & \boldsymbol{e}_m^P.\partial_{nn}\boldsymbol{x}_P \end{bmatrix} \tag{27}$$

is the *second fundamental form* [26]. The second fundamental form is used to characterise the local curvature of the road surface. The constraints on ω_x^b and ω_y^b are thus

$$\begin{bmatrix} -\omega_y^b \\ \omega_x^b \end{bmatrix} = J^{-1}(II)I^{-1}J \begin{bmatrix} u \\ v \end{bmatrix}. \tag{28}$$

3.3. Parametrisation for the Darlington Raceway

The track parametrisation given in (7) becomes unwieldy without the introduction of simplifying assumptions. These assumptions will be track-specific and are also motivated by the road model's eventual use. The legacy three-dimensional road model corresponds to the case $m(s,n) = 0$ [18,20,21].

The centre-line curvatures for the Darlington Raceway are shown in Figure 4. On the basis of this information, and other detailed knowledge of the track, we will neglect the following terms in subsequent calculations: $\partial_s m$, $\partial_{sn} m$, $\partial_{nn} m$, $\Omega_x\Omega_y m$, $\Omega_x^2 m$, $\Omega_y^2 m$, $\Omega_y\Omega_z m$, Ω_x^3, Ω_y^3, Ω_z^3, $\Omega_x^2\Omega_y$, $\Omega_y^2\Omega_z$, $(\partial_n m)^2$, and $m\partial_n m$. There is no suggestion that these assumptions are suitable for all tracks or that they are indeed even necessary.

It follows by direct calculation, using (7) and (2), that

$$\partial_s \boldsymbol{x}_P = (1 + \Omega_y m - n\Omega_z)\boldsymbol{t} - m\Omega_x \boldsymbol{n} + n\Omega_x \boldsymbol{m}, \tag{29}$$

$$\partial_n \boldsymbol{x}_P = \boldsymbol{n} + \boldsymbol{m}\partial_n m, \tag{30}$$

$$\begin{aligned} \partial_{ss}\boldsymbol{x}_P = {} & (m\partial_s\Omega_y - n\partial_s\Omega_z + \Omega_x(n\Omega_y + m\Omega_z))\boldsymbol{t} \\ & + (\Omega_z - m\partial_s\Omega_x - n(\Omega_x^2 + \Omega_z^2))\boldsymbol{n} \\ & + (n(\partial_s\Omega_x + \Omega_y\Omega_z) - \Omega_y)\boldsymbol{m}, \end{aligned} \tag{31}$$

$$\partial_{sn}\boldsymbol{x}_P = (\Omega_y\partial_n m - \Omega_z)\boldsymbol{t} + (-\Omega_x\partial_n m)\boldsymbol{n} + \Omega_x \boldsymbol{m}, \tag{32}$$

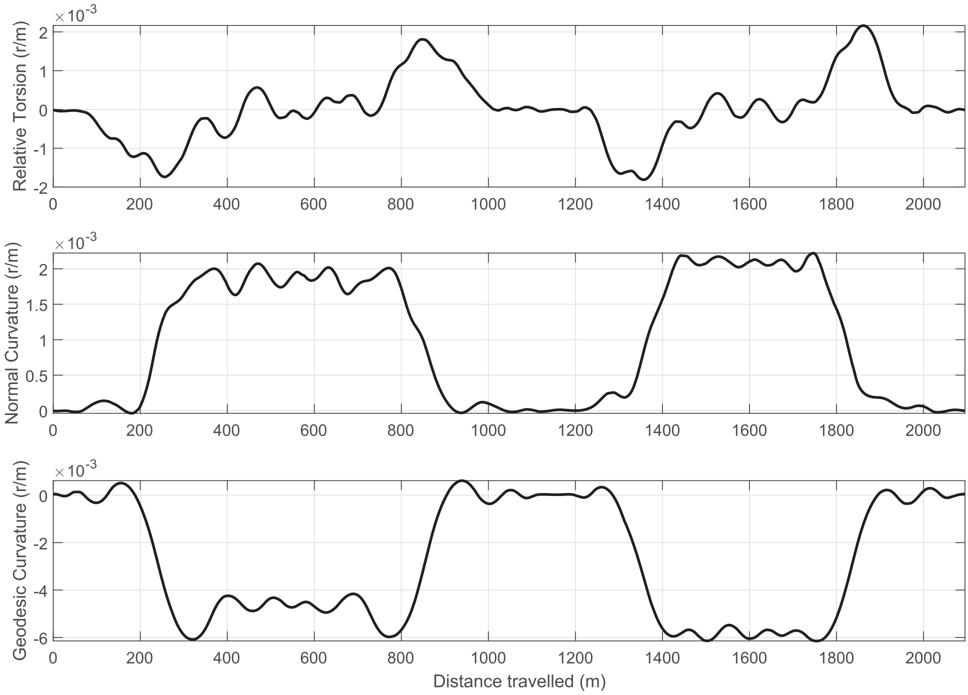

Figure 4. Centre-line curvatures for the Darlington Raceway.

$$\partial_{nn}\boldsymbol{x}_P = 0; \tag{33}$$

$\partial_s \boldsymbol{x}_P$ and $\partial_n \boldsymbol{x}_P$ are predominantly in the $\boldsymbol{t}$ and $\boldsymbol{n}$ directions, respectively.

The road-surface normal is given by

$$\boldsymbol{e}_m^P = \frac{-n\Omega_x \boldsymbol{t} + (\partial_n m(n\Omega_z - 1))\boldsymbol{n} + (1 + m\Omega_y - n\Omega_z)\boldsymbol{m}}{\sqrt{n^2\Omega_x^2 + (\partial_n m(n\Omega_z - 1))^2 + (1 + m\Omega_y - n\Omega_z)^2}}, \tag{34}$$

which follows from (8), and as expected, is predominantly in the $\boldsymbol{m}$-direction.

The car's heading co-angle comes from (16) and is given by

$$\dot{\xi} = \omega_z^b + \dot{s}\left(\frac{n(\Omega_x^2 + \Omega_z^2) - \Omega_z + \Omega_y \partial_n m(1 - n\Omega_z)}{\sqrt{n^2\Omega_x^2 + (1 - n\Omega_z)^2 + 2m\Omega_y}}\right). \tag{35}$$

This differential equation is used, because it is less cumbersome to work with than its counterpart (16). The heading and co-heading angles χ and ξ are related by

$$\chi = \arccos\left(\frac{\Omega_x(n\partial_n m - m)}{\sqrt{n^2\Omega_x^2 + (1 - n\Omega_z)^2 + 2m\Omega_y}}\right) - \frac{\pi}{2} + \xi; \tag{36}$$

$\chi \approx \xi$ when $n\partial_n m - m \approx 0$. This is the case for the Darlington track considered here, and consequently, (35) gives the car's heading angle.

The first fundamental form comes from (21) and is given by

$$I = \begin{bmatrix} n^2\Omega_x^2 + (1-n\Omega_z)^2 + 2m\Omega_y & \Omega_x(n\partial_n m - m) \\ \Omega_x(n\partial_n m - m) & 1 \end{bmatrix}, \tag{37}$$

where the influence of m is evident. Jacobian (22) is given by

$$J = \begin{bmatrix} \cos\chi\sqrt{n^2\Omega_x^2 + (1-n\Omega_z)^2 + 2m\Omega_y} & -\sin\chi\sqrt{n^2\Omega_x^2 + (1-n\Omega_z)^2 + 2m\Omega_y} \\ \sin\xi & \cos\xi \end{bmatrix}, \tag{38}$$

which allows (23) to be solved.

Second fundamental form (27) is given by

$$II = \frac{1}{a}\begin{bmatrix} n\partial_s\Omega_x + n^2(\Omega_x\partial_s\Omega_z - \Omega_z\partial_s\Omega_x) & \\ \quad +nm(\Omega_y\partial_s\Omega_x - \Omega_x\partial_s\Omega_y) - \Omega_y(1-n\Omega_z)^2 & f \\ f & 0 \end{bmatrix}, \tag{39}$$

where

$$a = \sqrt{n^2\Omega_x^2 + (1-n\Omega_z)^2 + 2m\Omega_y} \quad \text{and} \quad f = \Omega_x(1 - n\Omega_y\partial_n m) \approx \Omega_x,$$

which allows (28) to be solved.

Following [19], we use

$$m(s,n) = \sum_{j=2}^{J} a_j(s)n^j; \tag{40}$$

which was fitted to LiDAR track survey data; $J = 4$ was found to be adequate and was thus selected. Setting $a_0(s) = a_1(s) = 0$ forces the road surface to coincide with, and be tangent to, the Darboux frame's tangent plane along the centreline – see Figure 2(b). An optimisation process is used to compute $a_2(s)$, $a_3(s)$, $\partial_s a_2(s)$, and $\partial_s a_3(s)$, which allow the requisite partial derivatives relating to $m(s,n)$ to be computed [19].

It is worth re-emphasising that the simplifying assumptions made here are track and purpose dependent. In the case of the Darlington Raceway, $\partial_s m(s,n)$ can be neglected and so its higher derivatives can be neglected too. The peak values of all the curvatures are of the order 10^{-3} rad/m, with the peak values of their spatial derivatives of the order 10^{-5} rad/m^2. As one reduces the number of assumptions one is prepared to make, the more burdensome the calculations become. Figure 5 shows the track camber angle variations with lateral track position, which is a noteworthy facet of the Darlington raceway. The camber variations are most pronounced in Turns 2 (600–800 m) and 4 (1600–1800 m).

There are many ways in which one may parametrise a track given survey data of some sort. Possible candidates include algebraic functions (as was used here), B-spline patches, Bézier patches, NURBS patches, and so on. At this point, we are reliant on future research to establish the best way to parametrise general road surfaces, these too are possibly track dependent.

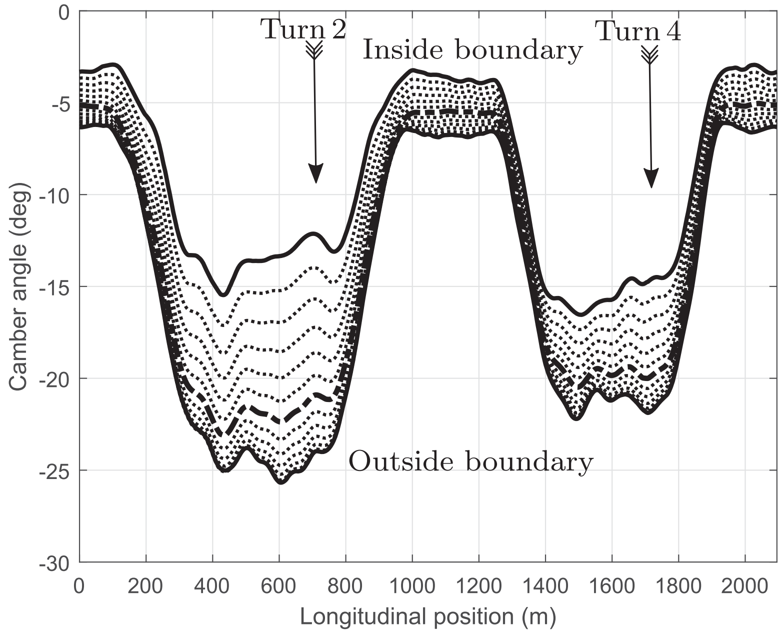

Figure 5. Darlington speedway camber variations with lateral and longitudinal positions. The track boundaries as shown solid with the centre line dot-dashed. The dotted lines are equi-spaced laterally and correspond to the survey data.

4. Car model

In this study, the car is modelled as a single rigid body and the vehicle's equations of motion are derived using standard Newton–Euler arguments. Using the notation detailed in [18], the external forces acting on the car in a car-fixed coordinate system are given by

$$F_x = (F_{frx} + F_{flx})\cos\delta - (F_{fry} + F_{fly})\sin\delta + F_{rrx} + F_{rlx} + G_x + F_{ax}, \tag{41}$$

$$F_y = (F_{fry} + F_{fly})\cos\delta + (F_{frx} + F_{flx})\sin\delta + F_{rry} + F_{rly} + G_y + F_{ay}, \tag{42}$$

$$F_z = F_{rrz} + F_{rlz} + F_{frz} + F_{flz} + G_z - F_{az}, \tag{43}$$

where G_x, G_y and G_z are projections of the gravitational force on to the body-fixed axes. Projecting the gravitational force along the $\partial_s \boldsymbol{x}^p$ and $\partial_n \boldsymbol{x}^p$ directions gives

$$\boldsymbol{G}_\perp = Mg\left(\frac{(\boldsymbol{e}_z^g.\partial_s \boldsymbol{x}_P)\partial_s \boldsymbol{x}_P}{\partial_s \boldsymbol{x}_P.\partial_s \boldsymbol{x}_P} + \frac{(\boldsymbol{e}_z^g.\partial_n \boldsymbol{x}_P)\partial_n \boldsymbol{x}_P}{\partial_n \boldsymbol{x}_P.\partial_n \boldsymbol{x}_P}\right),$$

so that $G_x = \boldsymbol{G}_\perp.\boldsymbol{e}_x^b$, $G_y = \boldsymbol{G}_\perp.\boldsymbol{e}_y^b$ and $G_z = Mg(\boldsymbol{e}_m^P.\boldsymbol{e}_z^b)$. The tyre-force modelling follows [18] with the parameters given in Appendix 2. The aerodynamic force components are given by F_{ax}, F_{ay} and F_{az} (see Appendix 3 for further details).

The external moments acting on the car are given by

$$M_x = w_r(F_{rlz} - F_{rrz}) + w_f(F_{flz} - F_{frz}) + h(F_y - G_y) + M_{ax}, \tag{44}$$

$$M_y = a(F_{frz} + F_{flz}) - b(F_{rrz} + F_{rlz}) - h(F_x - G_x) + M_{ay}, \tag{45}$$

$$M_z = a((F_{fry} + F_{fly})\cos\delta + (F_{frx} + F_{flx})\sin\delta) - b(F_{rry} + F_{rly}) + w_f((F_{flx} - F_{frx})\cos\delta + (F_{fry} - F_{fly}))\sin\delta + w_r(F_{rlx} - F_{rrx}) + M_{az}. \tag{46}$$

The aerodynamic moment components are given by M_{ax}, M_{ay} and M_{az} (see Appendix 3).

The two translational and one rotational freedoms of the car are described by

$$\dot{u} = (v + h\omega_x^b)\omega_z^b + h\dot{\omega}_y^b + F_x/M, \tag{47}$$

$$\dot{v} = (h\omega_y^b - u)\omega_z^b - h\dot{\omega}_x^b + F_y/M, \tag{48}$$

$$I_{zz}\dot{\omega}_z^b = M_z + (I_{xx} - I_{yy})\omega_x^b\omega_y^b. \tag{49}$$

In order to compute the individual tyre loads, we balance the forces acting on the car normal to the road, and then balance moments around the body-fixed $\boldsymbol{x}_x^b$ and $\boldsymbol{x}_x^b$ axes. A vertical force balance gives

$$0 = u\omega_y^b - v\omega_x^b - h((\omega_y^b)^2 + (\omega_x^b)^2) + F_z/M. \tag{50}$$

Moment balances around the car's longitudinal and lateral body-fixed axes give

$$I_{xx}\dot{\omega}_x^b = M_x + (I_{yy} - I_{zz})\omega_z^b\omega_y^b, \tag{51}$$

$$I_{yy}\dot{\omega}_y^b = M_y + (I_{zz} - I_{xx})\omega_z^b\omega_x^b. \tag{52}$$

The so-called fourth equation comes from a roll balance, which is described in Appendix 4 (see Equation (A14)). Kinematic constraints (23) and (28) are also required.

The car parameters are given in Appendix 2.

The aerodynamic forces and moments acting on the car are a function of the vehicle's speed and orientation relative to the road and air stream. In this study, the aerodynamic coefficients are modelled as functions of the chassis roll angle, the vehicle's side-slip angle, and the front and rear ride heights. This dependence (on four independent variables) is described in terms of multivariate polynomials that have been fitted to wind tunnel data. More details on the determination of the aerodynamic coefficients are given in Appendix 3. The aerodynamic loading on the car is sensitive to the chassis position and orientation relative to the road and air stream. Further details concerning the relationships between the tyre normal loads, the suspension stiffnesses and preloads, and the chassis positioning above the road are given in Appendix 4.

While the main dynamic model assumes a 'stiff' suspension, this assumption is relaxed in the context of the aerodynamic force and moment modelling. For these purposes, one can compute the chassis height, as well as its pitch and roll angles from the tyre normal loads, and the suspension stiffnesses and preload values (see Appendix 5 for these details).

5. Optimal control

This section describes briefly the essential features of the minimum-lap-time OCP. In our case, the vehicle's control inputs are

$$\mathbf{u} = [\ddot{\delta}, \dot{k}_{fr}, \dot{k}_{fl}, \dot{k}_{rr}, \dot{k}_{rl}, F_{frz}, F_{flz}, F_{rrz}, F_{rlz}], \tag{53}$$

where $\ddot{\delta}$ is the steering angular acceleration, $\dot{k}_{fr}$, $\dot{k}_{fl}$, $\dot{k}_{rr}$, and $\dot{k}_{rl}$ are the rates of change of the tyres' longitudinal slips (only braking is allowed on the front wheels), while F_{frz}, F_{flz}, F_{rrz}, and F_{rlz} are the tyre normal loads (which must remain negative so that the car remains on the road). The vehicle states are

$$\mathbf{x} = [u, v, n, \chi, \omega_z^b, \delta, \dot{\delta}, k_{fr}, k_{fl}, k_{rr}, k_{rl}]; \tag{54}$$

these quantities follow the notation given in [18]. The problem performance index is

$$\mathcal{J} = \oint (1 + \sum_1^5 R_i u_i^2(s) + R_{rtp} P_{rt}^2(s)) \mathrm{d}s,$$

in which the summation entry contains regularisation terms on the first five controls; the R_i's are 'tuned' by trial. The third term is a penalty on the rear tyres' lateral slip-related power loss that is given by

$$P_{rt} = (v - b\omega_z^b)(F_{rry} + F_{rly});$$

F_{rry} and F_{rly} are the rear tyre lateral tyre forces, with R_{rtp} another weight penalty chosen by trial. While $\mathcal{J}$ is predominantly the lap time (within $\pm$ 0.5%), the exact lap time can be computed by appending a 'time measuring' state to the state vector.

The inequality constraints include the maximum engine power constraint

$$P_{\max} - u(F_{rrx} + F_{rlx}) \geq 0.$$

The limited-slip differential constraint is

$$0 = (T_{rr} - T_{rl}) + K_{\text{diff}}(\omega_{rr} - \omega_{rl}),$$

while the brake balance constraint is

$$0 = B_{\text{bal}} \min(T_{fr} + T_{fl}, 0) - (1 - B_{\text{bal}}) \min(T_{rr} + T_{rl}, 0); \tag{55}$$

the wheel torques are given by

$$\begin{aligned} T_{fr} &= F_{frx} R_{fr}, \\ T_{fl} &= F_{flx} R_{fl}, \\ T_{rr} &= F_{rrx} R_{rr}, \\ T_{rl} &= F_{rlx} R_{rl}. \end{aligned}$$

The wheel radii are given by R_{fr} and so on. The minima in (55) ensure that the brake balance constraint only applies to braking torques. Constraints that ensure that the car remains on the track are

$$n - w_f \cos(\chi) + a \sin(\chi) - r_w/2 \geq 0, \tag{56}$$

$$n - w_r \cos(\chi) - b \sin(\chi) - r_w/2 \geq 0, \tag{57}$$

$$r_w/2 + n + w_f \cos(\chi) + a \sin(\chi) \leq 0, \tag{58}$$

$$r_w/2 + n + w_r \cos(\chi) - b \sin(\chi) \leq 0, \tag{59}$$

in which r_w is the (position-dependent) track width. The first two constraints ensure that no wheel touches the right-hand track boundary, while the second two constraints ensure the same for the left-hand boundary.

The OCP is solved using GPOPS-II [27], together with the NLP solver IPOPT [28]; all variables are scaled based on a reference length, a reference time, and a reference mass as described in [18].

6. Results

The purpose of this section is to compare the results from an industrial simulation tool, measured telemetry data captured during a race, and optimal control simulations using both laterally flat ($m(s,n) = 0$) and laterally curved ($m(s,n) \neq 0$) track models. The industrial simulation tool is a 182 DOF multibody model developed in Dymola/Modelica. The suspension model contains nonlinear springs, nonlinear dampers and bump stops, chassis and suspension compliances, and aerodynamic loading. The tyres are described by modified MF 6.1 tyre models [29]. The vehicle model is interfaced to a high-definition LiDAR scan of the racing surface (this is the same as the track model data used in Section 2). The model is controlled around the lap using a number of feed-forward and feedback controllers. The following nomenclature will be used on each of the plots: (i) the optimal control results with the laterally curved track will be shown solid; (ii) the optimal control results with the laterally flat track will be shown dot-dashed; (iii) the industrial simulation results will be shown dotted; and (iv) measured race results will be shown dashed.

Figure 6(a) and 6(b) show, respectively, the vehicle speed and engine power (throttle opening) for a single racing lap of the Darlington Raceway. The largest interval of divergence between the measured and the three simulated results occurs in Turns 1 and 2. On the entry to Turn 1, the measured speed is 1–3 m/s lower than all the simulation results. As the car travels through Turns 1 and 2 the best prediction came from the optimal control simulation with a laterally variable cambered track; the laterally flat simulation is too slow, while the industrial simulation speed prediction appears too fast. On the exit of Turn 2 both optimal control simulations provide reasonable speed prediction, although laterally flat prediction starts out too slow (relative to the measured data). This serves to highlight the deficiencies of a laterally-flat track model. The deceleration profiles into Turn 3 are comparable in all four cases. The best prediction of the car's speed in Turn 4 and its exit comes from the optimal simulation with a laterally curved track. The predicted exit speed of the industrial simulation is too fast, while the optimal control simulation with a laterally flat track is initially too slow. These speed profiles emphasise the fact that the laterally flat track does not allow the car to exploit the increased track camber found at the outside of the track in Turns 1 and 2, and then again in Turns 3 and 4 (see Figure 5). The associated lap times given in Table 1 are in good agreement. The engine power (throttle position) predicted by two simulations and the measured data are in broad agreement. That said, due to modelling deficiencies, the optimal control simulations might be losing an opportunity to apply full power at the 600 m mark, but both simulations are returning to full power slightly earlier than the industrial simulation and the measured race driver.

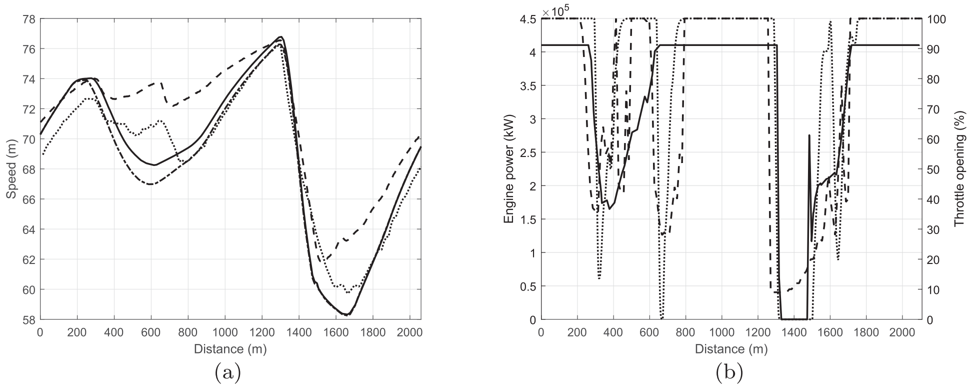

Figure 6. The (a) part of the figure shows the car's speed for the four cases described above. The (b) figure shows the engine power in the case of the optimal control simulations (left-hand axis), and the throttle opening (as a %) (right-hand axis) in the case of the measured behaviour and the industrial simulation.

Table 1. Lap times.

Measured	30.60 s
Industrial	29.78 s
Optimal – laterally flat	30.48 s
Optimal – laterally curved	30.63 s

The racing lines are compared in Figure 7. These figures show that the racing driver follows a racing line that is close to that predicted by the laterally curved optimal control and industrial simulations; the industrial tool includes a high-fidelity track model. In contrast, the laterally flat simulation (apparently incorrectly) follows a more conventional line that seeks to maximise the turning radius of curvature. The 'maximum radius of curvature' line is sub-optimal, because it does not exploit the benefits of the increased track cambering at the outside of the track (see Figure 5). Figure 7(b) emphasises the importance of a laterally curved track representation. The measured, optimal laterally curved, and industrial simulator predictions are in good agreement, while the laterally flat optimal control simulation emphasises (incorrectly) the use of the inside of the track in every turn.

Figure 8 shows the loading on each tyre during a racing lap; the industry-based simulation is compared with the optimal simulation with a laterally curved track model. The (a) part of the figure shows the normal loading on each tyre. It is evident that the loading on each tyre is roughly equal on the straight sections, while there is high loading on the right-hand tyres on the (left-hand) corners. The discrepancies between the two simulations are due predominantly to the simple tyre and suspension models used in the optimal control simulation. The (b) part of the figure shows the lateral loading on each tyre. In this case, the predictions made by each model are in good agreement. The bulk of the lateral loading is put on right-hand tyres as the car rolls out of the (left-handed) corners. The (c) part of the figure compares the longitudinal loading on each tyre; it is evident that there are only braking forces applied to the front tyres. As one would expect, the bulk of the drive power delivery comes from the rear-right tyre due to its high normal loading. Again, the longitudinal loading predictions for each model are in reasonable agreement,

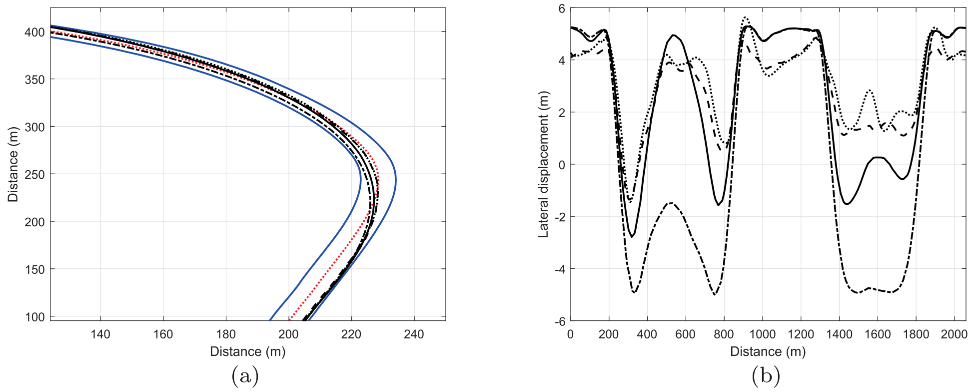

Figure 7. Optimal racing line. The (a) part of the figure shows the car's position in Turn 1 and the (b) part of the figure shows the car's lateral position relative to the centre line.

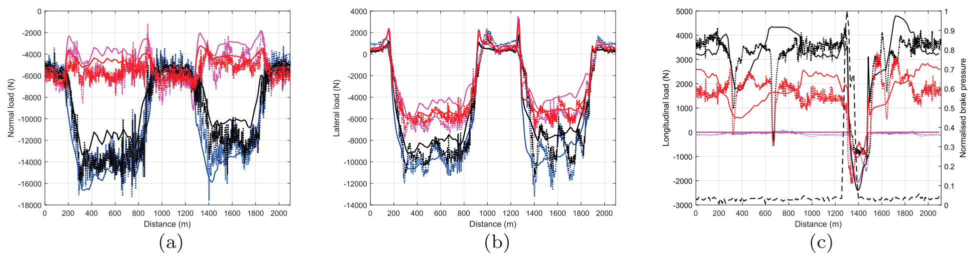

Figure 8. Normal, lateral and longitudinal tyre loads, and measured brake pressure. The industry-based simulation is shown dotted, while the optimal simulation with a laterally curved track is shown solid. The front-right tyre is blue, the front-left tyre is magenta, the rear-right tyre is black, while the rear-left tyre is shown red. (Colour online.)

with the industry-based simulation predicting 'dab braking' on the entry to Turns 1 and 2. Both models predict heavy braking on the entry to Turn 3 due to its tightening geodesic curvature; see Figure 4 at approximately 1300 m.

The remainder of the section will be devoted to the car's aerodynamic performance. Predictions of the aerodynamic loading on the car rely on the aero-coefficients derived from wind tunnel testing, which is covered in Appendix 3; see Equations (A7) to (A12) inclusive. The aerodynamic coefficients, in turn, are informed by the suspension setup and the car's side-slip behaviour. The suspension modelling and preload setup are detailed in Appendix 5. Figure 9 shows predictions from the industry simulator and the optimal control predictions based on a laterally curved track model.

The rear ride height is held at approximately 130 mm throughout the lap, but drops to approximately 115 mm in Turns 1 and 2. The front ride height is considerably lower and held at approximately 35 mm, with reductions to 25–30 mm in Turns 1 and 2. The two simulator predictions are in reasonably good agreement. The roll and side-slip angles are given in Figure 10. Again, the agreement between the two simulations is acceptable, although the industry-based simulation shows a more oscillatory response in both signals.

Having dealt with the signals that determine the aerodynamic coefficients, the resulting force components are shown in Figure 11. The (a) part of the figure shows the two drag

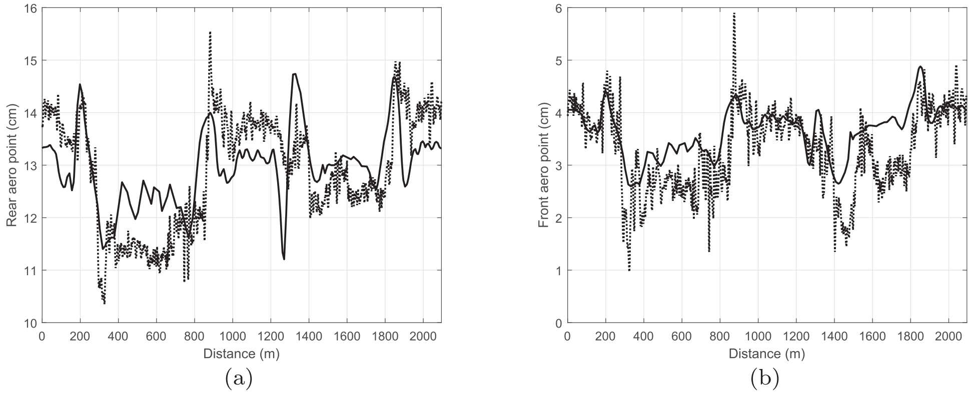

Figure 9. Front and rear ride heights. (a) The rear ride height is given by the average of the heights of chassis points P_3 and P_4 (see Figure A2). (b) The front ride height is the height of P_5.

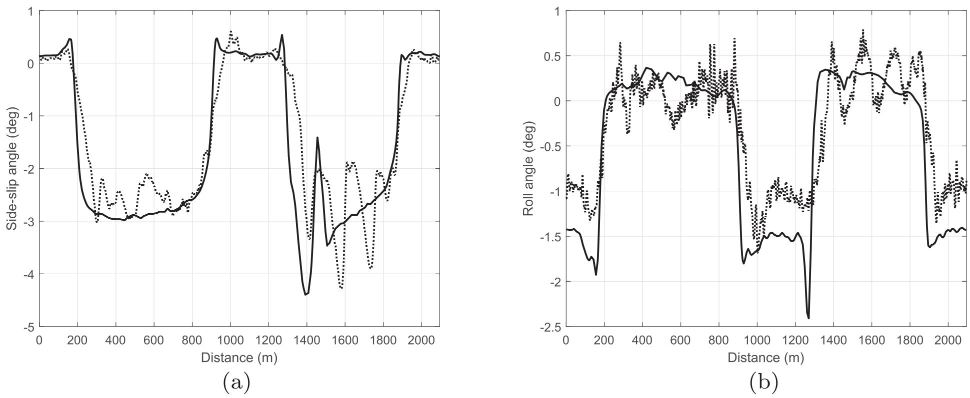

Figure 10. Side-slip and roll angles on the optimal racing line. (a) The simulated (solid) and industrial (dotted) slide-slip angles. (b) The simulated (solid) and industrial (dotted) roll angles.

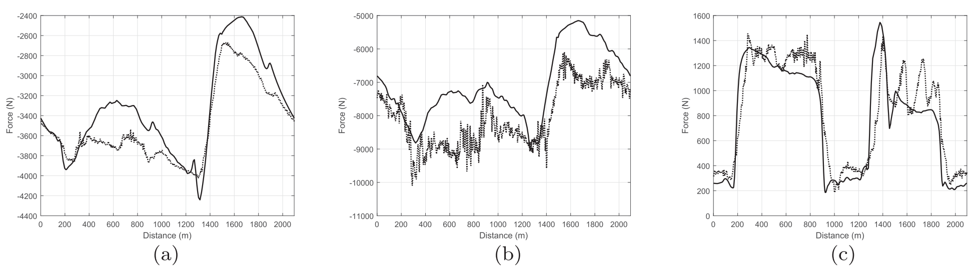

Figure 11. Optimal aerodynamic forces. (a) Drag, (b) downforce, and (c) side force; all in (N).

force predictions, which are in reasonably good agreement. That said, the optimal control simulation is under-predicting the drag in Turns 1 and 2, as well as on the entry to Turn 3. These differences are consistent with the speed difference there (see Figure 6(a)).

The downforce predictions are shown in the (b) part of the figure. Again, the optimal control-based simulation appears to be under-predicting the downforce in the four turns (relative to the industry-based simulator) as a result of the speed differences there. The (c) part of the figure shows the two side force predictions that are in good agreement – the industry-based simulation shows a more oscillatory response.

7. Conclusions

The purpose of this paper is to transfer and extend the minimum-lap-time simulation technologies developed in the context of Formula One to NASCAR. This technology transfer requires one to recognise the variable lateral curvature of some tracks as well as the various asymmetries of NASCAR-related race cars that are set up for oval tracks that are dominated by left-hand cornering. These asymmetries include different suspension characteristics on the left- and right-hand ends of each axle, four very different tyres as well as asymmetries in the car's aerodynamic behaviour. The results compare both simulation-based predictions and race-based telemetry data. For the most part, these various data sources are in good agreement, with the importance of variable lateral camber highlighted. It is shown how race car drivers on variable camber tracks have to find the best compromise between exploiting the additional camber on the outside of the track and increasing the travelled distance per lap combined with reductions in the cornering radius of turn. Other technology transfer demands can be expected in the future if NASCAR moves towards hybrid power trains. As was the case with Formula One, the challenges for manufacturers are expected to be remaining commercially relevant, maintaining the fan base, whilst also enhancing the sports 'green' credentials [30].

Note

1. If matrix D is non-singular, there holds

$$\begin{bmatrix} I & -BD^{-1} \\ 0 & I \end{bmatrix} \begin{bmatrix} A & B \\ C & D \end{bmatrix} \begin{bmatrix} I & 0 \\ -D^{-1}C & I \end{bmatrix} = \begin{bmatrix} A - BD^{-1}C & 0 \\ 0 & D \end{bmatrix}.$$

Disclosure statement

No potential conflict of interest was reported by the author(s).

ORCID

D. J. N. Limebeer http://orcid.org/0000-0002-3504-6290

References

[1] Scherenberg H. Mercedes-Benz racing design and cars experience. SAE Trans. 1958;66(580042): 414–420.
[2] Roland RD, Thelin CF. Computer simulation of Watkins Glen grand prix circuit performance. Cornell Aeronautical Laboratory; 1971. (Technical Report ZL-5002-K-1).
[3] Gadola M, Vetturi D, Cambiaghi D, et al. A tool for lap time simulation; 1996. (SAE Technical Papers).
[4] Braghin F, Cheli F, Melzi S, et al. Race driver model. Comput Struct. 2008;86(13–14): 1503–1516.

[5] Hatwal H, Mikulcik EC. Some inverse solutions to an automobile path-tracking problem with input control of steering and brakes. Veh Syst Dyn. 1986;15(2):61–71.
[6] Fujioka T, Kimura T. Numerical simulation of minimum-time cornering behavior. JSAE Rev. 1992;13(1):44–51.
[7] Wu AK, Miele A. Sequential conjugate gradient-restoration algorithm for optimal control problems with non-differential constraints and general boundary conditions, part I. Opt Control Appl Methods. 1980;1(1):69–88.
[8] Wu AK, Miele A. Sequential conjugate gradient-restoration algorithm for optimal control problems with non-differential constraints and general boundary conditions, part II. Opt Control Appl Methods. 1980;1(2):119–130.
[9] Hendrikx JPM, Meijlink TJJ, Kriens RFC. Application of optimal control theory to inverse simulation of car handling. Veh Syst Dyn. 1996;26(6):449–461.
[10] Kirk DE. Optimal control theory: an introduction. Englewood Cliffs (NJ): Prentice-Hall; 1970.
[11] Casanova D, Sharp RS, Symonds P. Minimum time manoeuvring: the significance of yaw inertia. Veh Syst Dyn. 2000;34(2):77–115.
[12] Kelly DP, Sharp RS. Time-optimal control of the race car: a numerical method to emulate the ideal driver. Veh Syst Dyn. 2010;48(12):1461–1474.
[13] Zhou JL, Tits AL, Lawrence CT. User's guide for FSQP version 3.0: a Fortran code for solving nonlinear (minimax) optimization problems, generating iterates satisfying all inequality and linear constraints. College Park (MD): Institute for Systems Research, University of Maryland; 1997. (Technical Report TR 92-107).
[14] Lovato S, Massaro M. A three-dimensional free-trajectory quasi-steady-state optimal-control method for minimum-lap-time of race vehicles. Veh Syst Dyn. 2021:1–19. doi:10.1080/00423114.2021.1878242.
[15] Lot R, Evangelou SA. Lap time optimization of a sports series hybrid electric vehicle. Proceedings of the world congress on engineering, Vol. III, London; 2013.
[16] Sharp RS, Peng Huei. Vehicle dynamics applications of optimal control theory. Veh Syst Dyn. 2011;49(7):1073–1111.
[17] Massaro M, Limebeer DJN. Minimum-lap-time optimization and simulation. Veh Syst Dyn. 2021;59(7):1069–1113.
[18] Limebeer DJN, Massaro M. Dynamics and optimal control of road vehicles. Oxford, UK: Oxford University Press; 2018.
[19] Lovato S, Massaro M, Limebeer DJ.N. Curved-ribbon-based track modelling for minimum lap-time optimisation. Meccanica. 2021;56:2139–2152.
[20] Limebeer DJN, Perantoni G. Optimal control of a formula one car on a three-dimensional track part 2: optimal control. ASME J Dyn Syst Meas Control. 2015;137(5). doi:10.1115/1.4029466 (13 pages).
[21] Perantoni G, Limebeer DJN. Optimal control of a formula one car on a three-dimensional track. Part 1: track modelling and identification. ASME J Dyn Syst Meas Control. 2015; 137(5). doi:10.1115/1.4028253 (11 pages).
[22] Fork T, Tseng HE, Borrelli F. Models and predictive control for nonplanar vehicle navigation; 2021. https://arxiv.org/abs/2104.08427.
[23] Rao AV, Benson DA, Darby C, et al. Algorithm 902: Gpops, a matlab software for solving multiple-phase optimal control problems using the gauss pseudospectral method. ACM Trans Math Softw (TOMS). 2010;37(2):1–39.
[24] Cossalter V, Da Lio M, Lot R, et al. A general method for the evaluation of vehicle manoeuvrability with special emphasis on motorcycles. Veh Syst Dyn. 1999;31(2):113–135.
[25] Arnold VI. Mathematical methods of classical mechanics. 2nd ed. New York: Springer; 2013.
[26] Kreyszig E. Differential geometry. 1st ed. New York: Dover; 2013.
[27] Patterson MA, Rao AV. GPOPS – II: a matlab software for solving multiple-phase optimal control problems using *hp*-adaptive Gaussian quadrature collocation methods and sparse nonlinear programming. ACM Trans Math Softw. 2014;41(1). doi:10.1145/2558904 (37 pages).
[28] Wächter A, Biegler LT. On the implementation of an interior-point filter line-search algorithm for large-scale nonlinear programming. Math Program. 2006;106:25–57.

[29] TNO Automotive. MF-tool 6.1 users manual; 2008.
[30] Trabesinger A. Power games. Nature. 2007;447:900–903.
[31] Perantoni G, Limebeer DJN. Optimal control of a formula one car with variable parameters. Veh Syst Dyn. 2014;52(5):653–678.
[32] Masouleh MI, Limebeer DJN. Optimizing the A–suspension interactions in a formula one car. IEEE Trans Control Syst Technol. 2016;24(3):912–927.

Appendices

Appendix 1: Changing the direction of rotation

When preparing the survey data in a track-curvature modelling exercise, the data should follow the track in a single contiguous direction. The survey direction need not be the running direction of the cars. In order to force the car to run in the correct direction, one need only to reverse the sign of either the x- or y-direction survey data. This does not change the track's geometry; see Figure A1. Flipping' the sign of the x- or y-axis data does no more than induce sign changes in the track curvature properties as detailed in Table A1.

Appendix 2: Vehicle and tyre parameters

This appendix contains the values of the vehicle and tyre parameters used in this study, with the vehicle parameters listed in Table A2. The tyre model and notation follow those given in [31], with the numerical values of each tyre parameter given in Table A3.

Appendix 3: Aerodynamic force modelling

The aerodynamic coefficients used in this study are represented by multivariate polynomials whose coefficients are fitted to measured wind tunnel data using least-squares. Four independent variables are used that correspond to (i) the height (f_{rh}) of the splitter given by point P_5 in Figure A2; (ii) the rear chassis height (r_{rh}) given by the average value of points P_3 and P_4; (iii) the chassis roll angle (φ) ; and (iv) the vehicle's side-slip angle (β). A similar approach to the aerodynamic modelling for a Formula One car is described in [32].

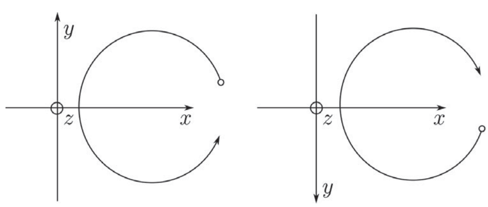

Figure A1. Effect of changing the car's running direction.

Table A1. Curvature and Euler angle sign changes for the opposing running direction.

$\delta(s) \to -\delta(s)$	$\tau(s) \to \tau(s)$	$\varphi(s) \to -\varphi(s)$[a]
$\dot\delta(s) \to -\dot\delta(s)$	$\dot\tau(s) \to \dot\tau(s)$	$\dot\varphi(s) \to -\dot\varphi(s)$
$\Omega_x(s) \to -\Omega_x(s)$	$\Omega_y(s) \to \Omega_y(s)$	$\Omega_z(s) \to -\Omega_z(s)$
$\dot\Omega_x(s) \to -\dot\Omega_x(s)$	$\dot\Omega_y(s) \to \dot\Omega_y(s)$	$\dot\Omega_z(s) \to -\dot\Omega_z(s)$
$a_2(s) \to a_2(s)$	$a_3(s) \to -a_3(s)$	$R_w(s) \to -R_w(s)$
$\dot a_2(s) \to \dot a_2(s)$	$\dot a_3(s) \to -\dot a_3(s)$	$\dot R_w(s) \to -\dot R_w(s)$

[a]Corrections of $\pm\pi$ radians may be required for some tracks.

Table A2. Vehicle parameters.

Symbol	Description	Value
g	Gravitational constant	9.81 m/s^2
M	Vehicle mass including driver	1552.20 kg
M_{fr}	Target corner masses for	445.14 kg
M_{fl}	Suspension set up	329.28 kg
M_{rr}	"	282.88 kg
M_{rl}	"	417.79 kg
I_{xx}	Vehicle moments of inertia	442.85 kg m^2
I_{yy}	"	2423.28 kg m^2
I_{zz}	"	2616.23 kg m^2
w	Vehicle length; See Figure A2	2.7895 m
a	See Figure A2	1.325 m
b	See Figure A2	1.465 m
h	Height of CoG	0.396 m
w_f	Front half-track width	0.778 m
w_r	Rear half-track width	0.783 m
R_{fr}	Wheel radius	0.364 m
R_{fl}	"	0.358 m
R_{rr}	"	0.361 m
R_{rl}	"	0.359 m
$P_{\max}$	Maximum engine power	410.135 kW
ρ	Air density	1.156 kg/m^3
A_f	Aerodynamic cross-sectional area	2.24 m^2
M_{arm}	Aerodynamic moment arm	2.794 m
P_1	Aero point; See Figure A2	[0.834898; 0.697738; 0.10033] m
P_2	"	[0.83439; −0.6971792; 0.08382] m
P_3	"	[−0.8127492; 0.6975856; 0.16637] m
P_4	"	[−0.8134096; −0.6989064; 0.1477772] m
P_5	"	[2.491486; 0.0004572; 0.0271272] m
P_6	"	[2.3992332; −0.5836666; 0.0195072] m
P_7	"	[2.3995634; 0.5846318; 0.0358648] m
B_{bal}	Brake balance	0.45
K_{diff}	Differential stiffness	2.5e4 Nms (locked differential)

Table A3. Tyre parameters.

Symbol	Front right	Front left	Rear right	Rear left
F_{z1}	−5524.54	−4472.44	−5254.62	−5019.47
F_{z2}	−13728.37	−6367.52	−13521.04	−6297.70
μ_{x1}	0.855517	1.14857	0.936367	1.160195
μ_{x2}	0.898665	1.18797	0.937544	1.186992
κ_1	0.046921	0.04789	0.051107	0.046764
κ_2	0.038575	0.04423	0.040467	0.044357
μ_{y1}	0.863775	1.29157	0.885916	1.198614
μ_{y2}	0.700057	1.29157	0.696319	1.065799
α_1	0.067888	0.05656	0.075406	0.055311
α_2	0.057476	0.04679	0.063077	0.050978
Q_x	1.498353	1.13194	1.496790	1.131497
Q_y	1.569762	1.34450	1.605538	1.362036

A *monomial* in n variables $x_1, \ldots, x_n$ is a product

$$x^a = x_1^{a_1} x_2^{a_2} \ldots x_n^{a_n},$$

in which the a_i's are non-negative integers. The degree of the monomial is $|a| = \sum_{i=1}^{n} a_i$. A polynomials in $x_1, \ldots, x_n$ given by

$$p(x) = \sum_{i=1}^{q} c_i x^a,$$

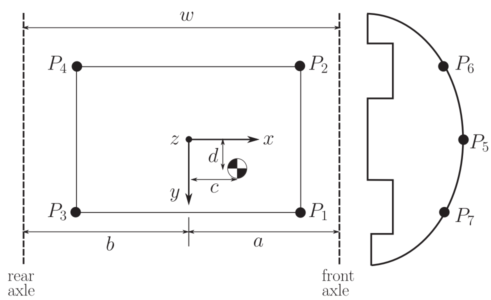

Figure A2. Chassis fixed points.

where the monomial coefficients c_i's are real numbers. The degree of the polynomial is the degree of the monomial of the highest degree. The number of monomials in n variables from degree 0 to degree d is given by $q = \frac{(n+d)!}{d!n!}$. We will order the monomials *Lexicographically*. If

$$a = \begin{bmatrix} a_1 & a_2 & a_3 & a_4 \end{bmatrix},$$

we say $x^a >_{lex} x^b$ if the difference $a-b$ and the leftmost non-zero entry are positive.

The least-squares fitting of multivariate polynomials to given data is an easy extension of the univariate case. Suppose that we wish to fit a multivariate polynomial of the form

$$\begin{bmatrix} 1 & x_1 & x_2 & \cdots & x_n^d \end{bmatrix} \begin{bmatrix} p_1 \\ p_2 \\ \vdots \\ p_q \end{bmatrix} \tag{A1}$$

to given data, in which the terms are listed in the lexicographic order. We assume that we have $k \geq q$ independent experimental outcomes, which can be stacked as

$$\begin{bmatrix} e_1 \\ e_2 \\ \vdots \\ e_k \end{bmatrix} = \begin{bmatrix} f_1 \\ f_2 \\ \vdots \\ f_k \end{bmatrix} - \overbrace{\begin{bmatrix} 1 & (x_1)_1 & (x_2)_1 & (x_3)_1 & \cdots & (x_n^d)_1 \\ 1 & (x_1)_2 & (x_2)_2 & (x_3)_2 & \cdots & (x_n^d)_2 \\ \vdots & & \ddots & \ddots & & \vdots \\ 1 & (x_1)_k & (x_2)_k & (x_3)_k & \cdots & (x_n^d)_k \end{bmatrix}}^{\Phi \in \mathbb{R}^{k \times q}} \begin{bmatrix} p_1 \\ p_2 \\ \vdots \\ p_q \end{bmatrix} \tag{A2}$$

in which $\mathbf{e}$ is a k-vector of errors, $\mathbf{f}$ is a k-vector of experiment outcomes, and $\mathbf{p}$ is a q-vector of monomial coefficients. More compactly

$$\mathbf{e} = \mathbf{f} - \Phi\mathbf{p}. \tag{A3}$$

By completing the square

$$\begin{aligned} \mathbf{e}^T\mathbf{e} &= (\mathbf{p} - (\Phi^T\Phi)^{-1}\Phi^T\mathbf{f})^T(\Phi^T\Phi)(\mathbf{p} - (\Phi^T\Phi)^{-1}\Phi^T\mathbf{f}) \\ &+ \mathbf{f}^T(I_k - \Phi(\Phi^T\Phi)^{-1}\Phi^T)\mathbf{f}. \end{aligned} \tag{A4}$$

Since both terms on the right-hand side of (A4) are non-negative for any choice of $\mathbf{p}$, with the second term independent of p, the optimal polynomial coefficients are given by

$$\mathbf{p}_{\text{opt}} = (\Phi^T\Phi)^{-1}\Phi^T\mathbf{f} \tag{A5}$$

with consequential RMS estimation error

$$\|\mathbf{e}\|_2 = \sqrt{\mathbf{f}^T(I_k - \Phi(\Phi^T\Phi)^{-1}\Phi^T)\mathbf{f}}. \tag{A6}$$

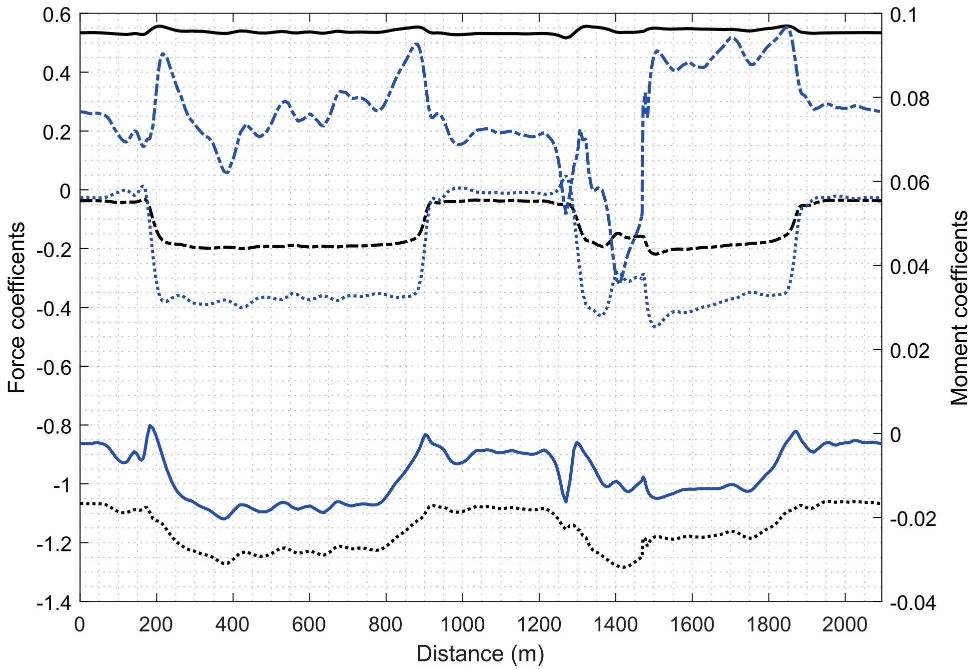

Figure A3. Aerodynamic coefficients for an optimal lap of the Darlington Raceway. The force coefficients are in black, while the moment coefficients are in blue. The x-axis is quantities are solid, the y-axis quantities are dot-dashed, and the z-axis quantities are dotted. (Colour online.)

In the specific case of relevance here

$$x^a = f_{rh}^{a_1} r_{rh}^{a_2} \varphi^{a_3} \beta^{a_4},$$

and we employed $n = 3$ to obtain $q = 35$ monomial coefficients for each coefficient. Actual numerical values have been withheld for commercial reasons, but the behaviour of these coefficients on an optimal lap can be seen in Figure A3.

The drag, side force, downforce and aerodynamic moments are given by

$$F_{ax} = \frac{\rho}{2} A_f CD_x u^2, \tag{A7}$$

$$F_{ay} = \frac{\rho}{2} A_f CD_y u^2, \tag{A8}$$

$$F_{az} = \frac{\rho}{2} A_f CD_z u^2, \tag{A9}$$

$$M_{ax} = \frac{\rho}{2} A_f CM_x M_{\text{arm}} u^2, \tag{A10}$$

$$M_{ay} = \frac{\rho}{2} A_f CM_y M_{\text{arm}} u^2, \tag{A11}$$

$$M_{az} = \frac{\rho}{2} A_f CM_z M_{\text{arm}} u^2, \tag{A12}$$

where ρ is the density of air, A_f is the car's cross-sectional area, u the vehicle's speed and M_{arm} the aerodynamic moment arm.

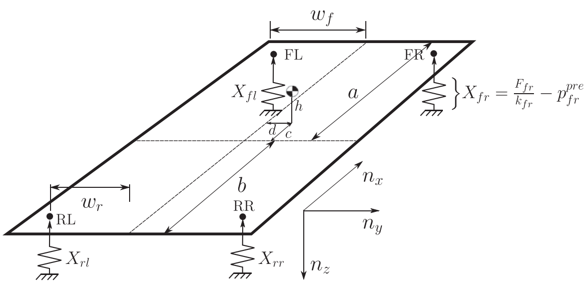

Figure A4. Rigid-chassis car with simple linear-spring suspension.

Appendix 4: Chassis posture

Figure A4 illustrates the geometric layout of a rigid-chassis car with its suspension. Each corner of the vehicle is assumed supported by a linear suspension (in the case of stiff suspensions with a small movement, this assumption is justifiable [32]). It is assumed that the spring displacements are perpendicular to the rigid planar chassis. The vertical displacement of the front-right wheel is given by $X_{fr} = \frac{F_{fr}}{k_{fr}} - p_{fr}^{pre}$, in which F_{fr} is the normal load, k_{fr} is the suspension stiffness, and p_{fr}^{pre} is the suspension preload. The other three wheels are treated in the same way. If the four suspension mounting points are co-planar, there holds

$$\frac{(X_{fl} - X_{fr})}{w_f} = \frac{(X_{rl} - X_{rr})}{w_r}, \tag{A13}$$

which is akin to saying that the front and rear axle roll angles are equal. For small angular displacements, the chassis roll angle is given by

$$\phi \approx \frac{(X_{fr} - X_{fl})}{2w_f} = \frac{(X_{rr} - X_{rl})}{2w_r}. \tag{A14}$$

Again, for small angles, the chassis pitch angle is given by

$$\theta \approx \left(\frac{(X_{rl} + X_{rr})/2 - \big((X_{fl} + X_{fr})/2\big)}{a + b} \right). \tag{A15}$$

When $a \approx b$, the chassis heave is given by

$$h \approx \frac{X_{fr} + X_{fl} + X_{rr} + X_{rl}}{4}. \tag{A16}$$

Appendix 5: Suspension preloads

We assume again that the chassis is rigid and that the wheel loads have been chosen so that the car is in equilibrium on the garage floor. The car is assumed to be driver-free. From Figure A4, the preloads and normal forces are related to the corner heave displacements by

$$F_{fr} = (X_{fr} + p_{fr})k_{fr}, \tag{A17}$$

$$F_{fl} = (X_{fl} + p_{fl})k_{fl}, \tag{A18}$$

$$F_{rr} = (X_{rr} + p_{rr})k_{rr}, \tag{A19}$$

$$F_{rl} = (X_{rl} + p_{rl})k_{rl}. \tag{A20}$$

In order for the external forces to be in equilibrium in the z-direction

$$0 = F_{fr} + F_{fl} + F_{rr} + F_{rl} - Mg, \tag{A21}$$

where M is the driver-less mass of the car. Balancing the moments due to the normal loads gives

$$\begin{aligned}
0 &= \begin{bmatrix} 0 & 0 & F_{fr} \end{bmatrix} \times \begin{bmatrix} a & w_f & -X_{fr} \end{bmatrix}' + \begin{bmatrix} 0 & 0 & F_{fl} \end{bmatrix} \times \begin{bmatrix} a & -w_f & -X_{fl} \end{bmatrix}' \\
&\quad + \begin{bmatrix} 0 & 0 & F_{rr} \end{bmatrix} \times \begin{bmatrix} -b & w_r & -X_{rr} \end{bmatrix}' + \begin{bmatrix} 0 & 0 & F_{rl} \end{bmatrix} \times \begin{bmatrix} -b & -w_r & -X_{rl} \end{bmatrix}' \\
&\quad + \begin{bmatrix} 0 & 0 & -Mg \end{bmatrix} \times \begin{bmatrix} c & d & h_{CG} \end{bmatrix}',
\end{aligned} \tag{A22}$$

where coordinates c, d, and h_{CG} define the car's mass centre. In component form

$$0 = \left(F_{fr} - F_{fl}\right) w_f + \left(F_{rr} - F_{rl}\right) w_r - dMg, \tag{A23}$$

$$0 = b\left(F_{rr} + F_{rl}\right) - a\left(F_{fr} + F_{fl}\right) + cMg, \tag{A24}$$

these equations represent lateral and longitudinal moment equilibria. Substituting (A17) to (A20) inclusive in (A23) and (A24) gives

$$\begin{aligned}
0 &= (X_{fr} + p_{fr})k_{fr}w_f - (X_{fl} + p_{fl})k_{fl}w_f + (X_{rr} + p_{rr})k_{rr}w_r \\
&\quad - (X_{rl} + p_{rl})k_{rl}w_r - dMg,
\end{aligned} \tag{A25}$$

$$\begin{aligned}
0 &= b\left((X_{rr} + p_{rr})K_{rr} + (X_{rl} + p_{rl})K_{rl}\right) - a\left((X_{fr} + p_{fr})K_{fr}\right. \\
&\quad \left. + (X_{fl} + p_{fl})K_{fl}\right) + Mg.
\end{aligned} \tag{A26}$$

Equations (A13), (A17) to (A20), (A21), (A25), and (A26) can be assembled into the following sets of eight equations

$$\begin{bmatrix} A_{11} & A_{12} \\ A_2 & A_2 \end{bmatrix} \begin{bmatrix} X \\ P \end{bmatrix} = \begin{bmatrix} L \\ F \end{bmatrix}, \tag{A27}$$

in which

$$X = \begin{bmatrix} X_{fr} \\ X_{fl} \\ X_{rr} \\ X_{rl} \end{bmatrix}, \quad P = \begin{bmatrix} p_{fr} \\ p_{fl} \\ p_{rr} \\ p_{rl} \end{bmatrix}, \quad L = \begin{bmatrix} 0 \\ Mg \\ dMg \\ -cMg \end{bmatrix}, \quad F = \begin{bmatrix} F_{fr} \\ F_{fl} \\ F_{rr} \\ F_{rl} \end{bmatrix}, \tag{A28}$$

where

$$A_{11} = \begin{bmatrix} -w_r & w_r & w_f & -w_f \\ k_{fr} & k_{fl} & k_{rr} & k_{rl} \\ k_{fr}w_f & -k_{fl}w_f & k_{rr}w_r & -k_{rl}w_r \\ -ak_{fr} & -ak_{fl} & bk_{rr} & k_{rl} \end{bmatrix}, \tag{A29}$$

$$A_{12} = \begin{bmatrix} 0 & 0 & 0 & 0 \\ k_{fr} & k_{fl} & k_{rr} & k_{rl} \\ k_{fr}w_f & -k_{fl}w_f & k_{rr}w_r & -k_{rl}w_r \\ -ak_{fr} & -ak_{fl} & bk_{rr} & bk_{rl} \end{bmatrix}, \tag{A30}$$

$$A_2 = \begin{bmatrix} k_{fr} & 0 & 0 & 0 \\ 0 & k_{fl} & 0 & 0 \\ 0 & 0 & k_{rr} & 0 \\ 0 & 0 & 0 & k_{rl} \end{bmatrix}. \tag{A31}$$

Since

$$\det(A_{11}) = -2(a+b)\left(w_f^2 k_{fr}k_{fl}(k_{rr} + k_{rl}) + w_r^2 k_{rr}k_{rl}(k_{fr} + k_{fl})\right),$$

A_{11} and A_2 are nonsingular for any realistic data set; however, both A and A_{12} are singular. Standard transformations based on Schur complements[1] allows (A27) to be replaced by

$$\begin{bmatrix} A_{11}-A_{12} & 0 \\ 0 & A_2 \end{bmatrix}\begin{bmatrix} X \\ P+X \end{bmatrix} = \begin{bmatrix} L-A_{12}A_2^{-1}F \\ F \end{bmatrix} \tag{A32}$$

with

$$A_{11}-A_{12} = \begin{bmatrix} -w_r & w_r & w_f & -w_f \\ 0 & 0 & 0 & 0 \\ 0 & 0 & 0 & 0 \\ 0 & 0 & 0 & 0 \end{bmatrix} \tag{A33}$$

and

$$L-A_{12}A_2^{-1}F = \begin{bmatrix} 0 \\ Mg-F_{fr}-F_{fl}-F_{rr}-F_{rl} \\ w_f(F_{fr}-F_{fl})+w_r(F_{rr}-F_{rl})-dMg \\ a(F_{fr}+F_{fl})-b(F_{rr}+F_{rl})-cMg \end{bmatrix}. \tag{A34}$$

For a solution to exist

$$0 = w_r(X_{fr}-X_{fl})-w_f(X_{rr}-X_{rl}), \tag{A35}$$

$$0 = Mg-F_{fr}-F_{fl}-F_{rr}-F_{rl}, \tag{A36}$$

$$0 = w_f(F_{fr}-F_{fl})+w_r(F_{rr}-F_{rl})-dMg, \tag{A37}$$

$$0 = a(F_{fr}+F_{fl})-b(F_{rr}+F_{rl})-cMg \tag{A38}$$

must hold. The first equation is simply a re-affirmation of co-planarity necessary condition (A13). The second equation is a re-affirmation of the vertical load balance condition (A21). The second, third and fourth equations provide conditions on the *CoG* offset in order to obtain pitch and roll moment equilibria. If (A34) is satisfied, (A27) may have multiple solutions.

In order to solve (A27), we suppose that

$$A_{12}P = \begin{bmatrix} 0 & 0 & 0 & 0 \\ k_{fr} & k_{fl} & k_{rr} & k_{rl} \\ k_{fr}w_f & -k_{fl}w_f & k_{rr}w_r & -k_{rl}w_r \\ -ak_{fr} & -ak_{fl} & bk_{rr} & bk_{rl} \end{bmatrix}\begin{bmatrix} p_{fr} \\ p_{fl} \\ p_{rr} \\ p_{rl} \end{bmatrix} = 0. \tag{A39}$$

The motivation for this proposal is clear. These equations say that the preloads, whatever they might be, must lead to a new equilibrium state. The second equation assets that the preloads make no net contribution the vertical force balance, while the third and fourth equations assert the same in respect of the roll and pitch moments, respectively. With (A39) in place, one obtains

$$X = A_{11}^{-1}L, \tag{A40}$$

and consequently,

$$P = A_2^{-1}F - A_{11}^{-1}L. \tag{A41}$$

As a check

$$A_{12}P = A_{12}(A_2^{-1}F - A_{11}^{-1}L) = A_{12}A_2^{-1}F - L = (A34) = 0, \tag{A42}$$

which shows that this set of preload adjustments is indeed an equilibrium solution. Of computational benefit is the fact that static displacements and preload calculations can be decoupled.

For the data given in Table A2, the *CoG* offset can be computed using (A37) and (A38). This gives

$$c = 0.0 \quad d = -0.0105.$$

Equations (A40) and (A41) can be solved to determine:

$$\begin{bmatrix} X_{fr} \\ X_{fl} \\ X_{rr} \\ X_{rl} \end{bmatrix} = \begin{bmatrix} 0.0097592045181563 \\ 0.0367479785516636 \\ 0.0219149014210898 \\ 0.0490871096396277 \end{bmatrix}, \quad \begin{bmatrix} p_{fr} \\ p_{fl} \\ p_{rr} \\ p_{rl} \end{bmatrix} = \begin{bmatrix} +0.00574605405375 \\ -0.01226528258583 \\ -0.00803785711365 \\ +0.03167264562873 \end{bmatrix};$$

the suspension displacements and preloads are all given in metres.